Title

Exploring the Effects of Intersubunit Interface Mutations on Virus-Like Particle Structure and Stability.

Authors

Pistono, Paige
Xu, Junyi
Huang, Paul
et al.

Publication Date

2024-07-22

DOI

10.1021/acs.biochem.4c00225

Peer reviewed

Biochemistry

pubs.acs.org/biochemistry
Article

Exploring the Effects of Intersubunit Interface Mutations on Virus-Like Particle Structure and Stability

Published as part of Biochemistry virtual special issue "Drug Delivery".

Paige E. Pistono, Junyi Xu, Paul Huang, Jennifer L. Fetzer, and Matthew B. Francis*

Cite This: *Biochemistry* 2024, 63, 1913−1924

ABSTRACT: Virus-like particles (VLPs) from bacteriophage MS2 provide a platform to study protein self-assembly and create engineered systems for drug delivery. Here, we aim to understand the impact of intersubunit interface mutations on the local and global structure and function of MS2-based VLPs. In previous work, our lab identified locally supercharged double mutants [T71K/G73R] that concentrate positive charge at capsid pores, enhancing uptake into mammalian cells. To study the effects of particle size on cellular internalization, we combined these double mutants with a single point mutation [S37P] that was previously reported to switch particle geometry from $T = 3$ to $T = 1$ icosahedral symmetry. These new variants retained their enhanced cellular uptake activity and could deliver small-molecule drugs with efficacy levels similar to our first-generation capsids. Surprisingly, these engineered triple mutants exhibit increased thermostability and unexpected geometry, producing $T = 3$ particles instead of the anticipated $T = 1$ assemblies. Transmission electron microscopy revealed various capsid assembly states, including wild-type ($T = 3$), $T = 1$, and rod-like particles, that could be accessed using different combinations of these point mutations. Molecular dynamics experiments recapitulated the structural rationale *in silico* for the single point mutation [S37P] forming a $T = 1$ virus-like particle and showed that this assembly state was not favored when combined with mutations that favor rod-like architectures. Through this work, we investigated how interdimer interface dynamics influence VLP size and morphology and how these properties affect particle function in applications such as drug delivery.

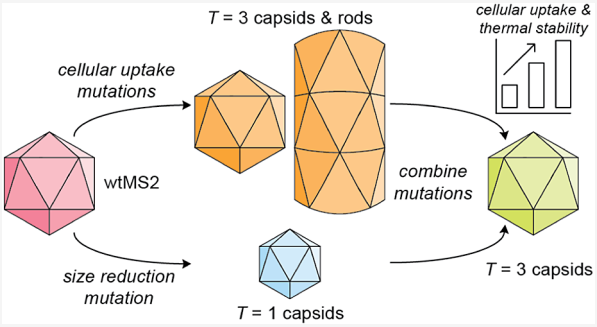

INTRODUCTION

Understanding the fundamental governing interactions present in protein self-assembly is important because proteins in supramolecular complexes perform many biological functions. Here, we discuss the engineering of a virus-like particle (VLP) to produce hollow protein shells with varying sizes, stabilities, and biological functions. VLPs are useful nanoparticles for the study of self-assembly and for the encapsulation and delivery of bioactive molecules, often enhancing their activity. VLPs are promising materials for use in drug delivery that (1) can be produced inexpensively by recombinant expression, (2) are homogeneous in size, and (3) are easily degraded in the body.[1,2] Self-assembling protein materials can be genetically engineered and chemically modified with new functionalities using site-selective bioconjugation reactions.[3−7] The functional organizations of many virus-like particles are icosahedra whose assembly geometries are governed by genetic economy and quasi-equivalence. Thus, a viral genome favors symmetric architectures with reduced coding cost, and many copies of a single protein monomer can adopt locally equivalent positions in a capsid; this allows viruses with larger sizes to form from increased numbers of building blocks.[8,9]

Several studies have found that VLP mutations can alter these assembly states, yielding particles with distinct or mixed assembly geometries. For example, Qβ VLPs possess natural variation in assembly geometry, as particle sizes from prolate to $T = 4$ particles are made along with infectious $T = 3$ virions.[10] It has also been shown that MS2 VLPs can naturally form a mix of $T = 3$ and $T = 4$ structures. However, many of these alternative assembly states are noninfectious in phage form because they do not possess the standard maturation protein incorporation site.[11] The sizes and shapes of various icosahedral VLPs can also be disrupted via loop insertion mutations, resulting in diverse forms of particles, including rod-like structures.[12−14]

MS2 is a well-studied bacteriophage that assembles into 27 nm, $T = 3$ icosahedral particles made up of 180 identical

Received: April 29, 2024
Revised: July 11, 2024
Accepted: July 12, 2024
Published: July 22, 2024

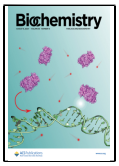

https://doi.org/10.1021/acs.biochem.4c00225
Biochemistry 2024, 63, 1913−1924

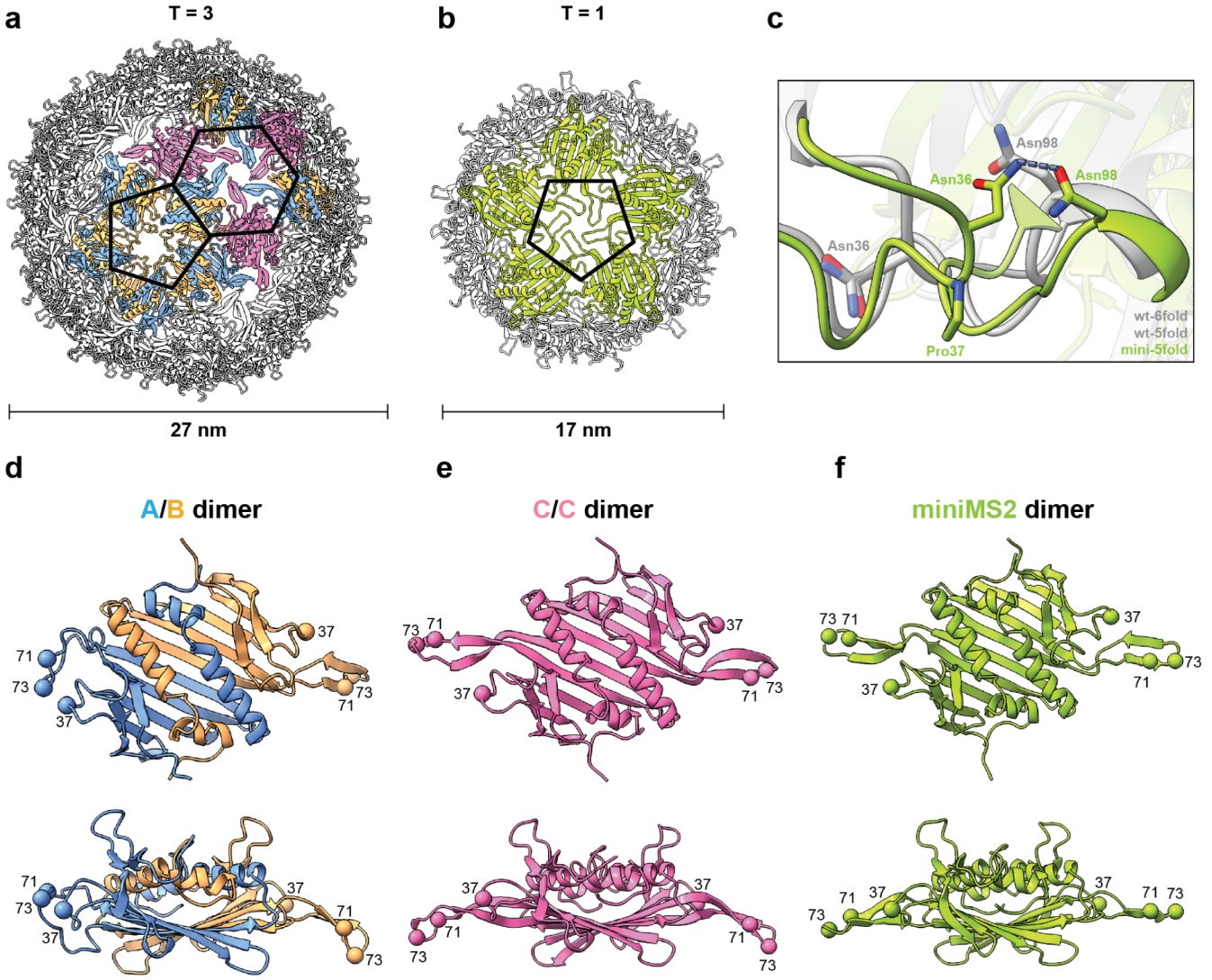

Figure 1. (A) Structure of wild-type MS2 capsid (PDB ID: 2MS2), shown, with A/B dimers (blue and yellow) and C/C dimers (pink) labeled. Five sets of A/B dimers assemble at the 5-fold interface (black pentagon), and three sets of A/B dimers alternating with three sets of C/C dimers assemble at the 6-fold interface (black hexagon). (B) Structure of the MS2[S37P], or "miniMS2" capsid (PDB ID: 4ZOR) shown, with dimers labeled in green. Five sets of dimers assemble at the 5-fold interface (black pentagon). (C) Interdimer interface interactions between residues Asn36 and Asn98 at the MS2 assembly interfaces are shown. The miniMS2 structure (green) is overlaid on the wtMS2 structures (gray). A key H-bonding interaction between the Asn36 side chain nitrogen and the Asn98 side chain oxygen at the miniMS2 interdimer interface is drawn as a blue dashed line. (D)−(F) Top and side views of the wtMS2 A/B dimer (blue and yellow), wtMS2 C/C dimer (pink), and miniMS2 dimer (green), respectively, with residues 37, 71, and 73 labeled as spheres.

monomers, which are folded into asymmetric A/B dimers and symmetric C/C dimers.[15] This conformational change occurs upon binding of genetic material to the dimer interior and allows for the formation of a $T = 3$ capsid with 5-fold, 3-fold (quasi 6-fold), and 2-fold assembly interfaces. Coincident with the 3-fold axes are hexameric interfaces with alternating sets of A/B and C/C dimers, while the 5-fold axes are made up of five sets of A/B dimers. MS2 can be recombinantly expressed, and deep mutational scanning techniques have been developed to characterize how individual amino acid mutations affect its assembly properties.[16] Studies have identified capsid variants with high assembly competency, thermostability, acid sensitivity, chemical modifiability, cell permeability, and mutations that alter particle size.[4,16−20]

In our recent study, we used the nanoscale assembly of MS2-based VLPs to create locally supercharged variants, thus enhancing their uptake into mammalian cells.[19] We identified two key double mutants that concentrated positive charge at capsid pores. The low cytotoxic and hemolytic activity of these variants and their ability to internalize into multiple cell types add to their promise as potential drug delivery vehicles. While these capsids were found to be stable in initial experiments, we noted that losses in stability over long-term storage periods occurred.

Work in the Tullman-Ercek lab previously identified MS2 S37P as a size-reducing mutation that mediates a switch in particle geometry from the native $T = 3$ capsid to a smaller, 17 nm $T = 1$ capsid comprising 60 symmetrically identical monomers (Figure 1A,B).[17] From structural data, they hypothesized that hydrogen bonding interactions between N36 and N98 were more favored in the MS2 S37P capsid, favoring stability at the 5-fold interface and creating a smaller particle (Figure 1C). Further work to identify self-assembly rules for shifting MS2 particle size showed that the identity of both

https://doi.org/10.1021/acs.biochem.4c00225
Biochemistry 2024, 63, 1913−1924

residues 36 and 37 was important for miniMS2 formation, and this design rule was applied to create smaller particles in MS2 homologue Qβ.[21]

MS2 S37P (herein referred to as "miniMS2") could serve as a valuable tool to study the effects of particle size on cellular uptake. Moreover, we reasoned that we could use the S37P mutation to determine if the previously identified uptake-enhancing mutations at positions 71 and 73 would work for particles of different sizes. We observed a delicate balance that governs particle assembly when combining mutations that favor stability at the 5-fold versus 6-fold assembly interfaces. Here, we report the discovery that specific mutations at the FG loop disrupt $T = 3$ icosahedron assembly and result in the formation of rod-like structures that are presumed to be comprised exclusively of 6-fold assembly interfaces. When combined with the 5-fold-favoring S37P mutation, we see a shift in particle assembly state back to $T = 3$, but do not observe the anticipated $T = 1$ particles. We also found that these combined mutations effectively delivered charged therapeutic cargo into mammalian cells. Moreover, combining these mutations resulted in particles with highly increased thermostability compared to the original locally supercharged double mutants.

MATERIALS AND METHODS

Cloning Procedure. MS2 variants with mutations at positions 71 and 73 were previously generated with EMPIRIC cloning.[22,23] Two single-stranded DNA primers were purchased, resuspended, and diluted to 5 μM for S37P site-directed mutagenesis. Site-directed mutagenesis was performed according to the protocols defined in the QuikChange Lightning Instruction Manual. Mutant strand synthesis was performed, and methylated template DNA was digested with DpnI. Amplification products were transformed into chemically competent *E. coli* DH10B cells. Cells were plated onto LB agar plates containing 32 μg/mL chloramphenicol and grown overnight at 37 °C. Individual colonies were picked and grown overnight in 2xYT media containing 32 μg/mL chloramphenicol at 37 °C, then plasmid DNA was isolated by Zyppy plasmid miniprep kit and sent for sequencing with pBAD forward and pBAD reverse sequencing primers.

Expression and Purification of Proteins. Overnight cultures of each MS2 variant were subcultured 1:200 into 1 L of 2xYT media containing 32 μg/mL chloramphenicol and grown to an OD_{600} of 0.4−0.6, then induced with 0.1% w/v arabinose. Proteins were expressed overnight at 37 °C with 220 rpm shaking, then cells were harvested by centrifugation and lysed by sonication. MS2 capsids were precipitated with two rounds of 50% saturated ammonium sulfate. Large-scale expressions of well-assembled MS2 variants were purified via FPLC on two HiScreen Capto Core 700 columns connected in series via isocratic flow with 10 mM phosphate buffer at pH 7.4 with 2 mM sodium azide as the equilibration, wash, and elution buffer, and 1 M NaOH in 30% isopropanol as the cleaning-in-place buffer. Some MS2 variants with cationic mutations were purified via affinity chromatography with a 5 mL HiTrap Heparin HP affinity column with 10 mM phosphate buffer at pH 7.4 with 2 mM sodium azide as the equilibration and wash buffer, and 2 M NaCl as the elution buffer.

Determination of Assembly State. The assembly state of each MS2 variant was characterized via HPLC size exclusion chromatography with an Agilent bioSEC-5 column (5 μm, 2000 Å, 7.8 × 300 mm^2) with isocratic flow of 10 mM phosphate buffer at pH 7.4 with 2 mM sodium azide. Coelution of A_{260} and A_{280} peaks at 6 min are indicative of $T = 3$ assembled capsids and at 8 min for $T = 1$ assembled capsids, while a peak at 10 min corresponds to the elution of unassembled MS2 dimers.

Mass Spectrometry. Modified and unmodified MS2 CP variants were analyzed with an Agilent 1260 series liquid chromatograph connected in-line with an Agilent 6530 LC/QTOF mass spectrometer with an electrospray ionization source. The expected mass of each MS2 CP variant was confirmed via QTOF-ESI-MS (Figure S1, Table S1).

Dye Modification. All MS2 CP variants containing the N87C mutation (final concentration 10 μM) were mixed with 5 equiv of Lissamine rhodamine B C2 maleimide (stock solution 5 mM in DMSO, 50 μM final concentration) in 10 mM phosphate buffer, pH 7.2. The solution was incubated on a rotator at room temperature for 1 h or at 4 °C overnight. Excess dye was removed by three rounds of washes through Amicon Ultra-0.5 mL 100 kDa MWCO filters and two rounds of filtration through Microspin G-25 columns. Modification of MS2 CP variants was verified via QTOF-ESI-MS and SDS-PAGE. The concentration of each MS2-fluorophore conjugate (MS2-Rho) was normalized to 5 μM for subsequent internalization assays (Figures S2 and S3).

Synthesis of MMAF-Conjugated MS2 Capsids. Samples of each MS2 construct were prepared at 20 μM and combined with 10 equiv of a stock solution of MC-Val-Cit-PAB-MMAF (Broadpharm) in 100 mM phosphate buffer (1% v/v DMSO) pH 7.4 and incubated overnight at 4 °C. Excess MMAF was removed via 7 cycles of spin filtration through a 100 kDa MWCO filter (Amicon), and product was analyzed by QTOF-ESI-MS (Figure S5, Table S3).

MTS Cell Viability Assay. An MTS Assay Kit (ab197010) was used according to Abcam's instructions to quantify cell viability after treatment with different MS2 CP variants. Briefly, an MTS tetrazolium compound is reduced by viable mammalian cells to generate a colored formazan dye that can be measured by absorbance at 490 nm. U-251 MG cells were plated into a 96-well plate at a concentration of 5,000 cells per well in 100 μL DMEM + FBS and incubated overnight at 37 °C with 5% CO_2. The next day, media was aspirated and replaced with 100 μL of either 0, 1, 5, 10, 20, or 40 μM MS2 diluted in DMEM + FBS and incubated for 24, 48, or 72 h at 37 °C with 5% CO_2. Then, the treatment media was aspirated and 100 μL DMEM + 20% MTS reagent was added to each well and incubated for 1 h at 37 °C with 5% CO_2 before measuring the absorbance at 490 nm. Cell viability was calculated as an absorbance percentage over the untreated control (eq 1).

$$\%\ \text{viability} = 100 \times \frac{\text{A490 treated cells}}{\text{A490 control cells}} \quad (1)$$

MS2-MMAE MTS Cell Viability Assay. U-251 MG cells were plated in a 96-well plate at 4,000 cells/well and allowed to adhere overnight. Cells were then incubated for 72 h at 37 °C with 80 μL DMEM + 10% FBS and 20 μL MS2-MMAE or vehicle control at appropriate concentrations in DPBS. Media were then aspirated and replaced with 200 μL prewarmed DMEM without phenol red or FBS along with 20 μL Abcam MTS Cell Proliferation Assay solution. Samples were then incubated in the dark for 1 h and immediately analyzed for optical density at 490 nm. Cell viability was calculated as an absorbance percentage over the untreated control (eq 1).

Mammalian Cell Culture. U-251 MG cells were cultured in DMEM supplemented with 10% fetal bovine serum (FBS), 4.5 g/L glucose, 4 mM L-glutamine, and 1 mM sodium pyruvate. All

https://doi.org/10.1021/acs.biochem.4c00225
Biochemistry 2024, 63, 1913−1924

cell cultures were maintained at 37 °C in a humidified atmosphere with 5% CO_2.

Flow Cytometry. A suspension of 80,000 U-251 MG cells were plated in each well of a 24-well plate and incubated overnight at 37 °C with 5% CO_2. Cells were washed three times with DPBS and treated with 5 μM MS2-Rho in DPBS with 1% FBS for 1 h at 37 °C with 5% CO_2. After incubation, cells were washed twice with DPBS. Cells were lifted with trypsin, quenched with FBS-containing DMEM and pelleted at 200 x *g* for 3 min. Cells were washed twice with DPBS and resuspended in 1 mL of DPBS. Cells were pelleted at 200 x *g* for 3 min and resuspended in 1 mL 2% paraformaldehyde with 0.1 μg/mL Hoechst 33 342 and kept at 4 °C until flow cytometry analysis. Flow cytometry was completed using an Attune NxT flow cytometer. At least 10,000 cells were analyzed for each sample. Data were analyzed using FlowJo and the mean fluorescence values with coefficient of variation were reported (Figure S4, Table S2). Fluorescence intensity values were corrected according to the % Rho modification of each MS2 CP variant.

Generation of S37P MS2 Structural Models. A T = 1 model of S37P MS2 containing all amino acid residues was generated based on the crystal structure of S37P MS2 (PDB ID: 4ZOR).[17] The missing loop regions of this structure were added using the Homology Modeling tool in Maestro (version 22.2) using 4ZOR as a template. Copies of the resulting homology model were then position aligned with five pentameric monomers of 4ZOR using the Align tool in PyMOL (version 3.0.0). The resulting pentamers were converted into the full 60-mer using the Multiscale Models tool in UCSF Chimera (version 1.17.3). Segments of this capsid comprising 20 monomers surrounding the 5-fold symmetry axes were then used in molecular dynamics simulations. A T = 3 model of S37P MS2 containing all amino acid residues was generated based on the crystal structure of wtMS2 (PDB ID: 2MS2).[24]

To enable rapid and simultaneous computations of MS2 variants with different combinations of mutations, smaller assemblies were created based on segments of the full T = 1 and T = 3 capsid assemblies. To represent the T = 1 capsid, a segment of ten sets of S37P MS2 CP (coat protein) dimers assembled at the 5-fold interface (4ZOR-10CP2, from PDB ID: 4ZOR) was used (Figure 4A–C). To represent the T = 3 capsid, a similar segment of ten sets of wtMS2 CP dimers assembled at the 5-fold interface (10CP2, from PDB ID: 2MS2) and an alternative segment of six sets of wtMS2 coat protein dimers (CP2) at the 6-fold assembly interface (2MS2–6CP2, starting from PDB ID: 2MS2) were used (Figure 4A–C). As noted in Figure 4, T = 1 MS2 lacks 6-fold interfaces. Initial structure preparation was conducted using Schrodinger Maestro suite (version 2022-2). Subsequent MS2 variants used in simulations were created using the Mutate tool in Maestro, then performing a short minimization with an OPLS4 force field to relax the structure around the mutation sites.

Molecular Dynamics Simulations. Molecular dynamics simulations were carried out using Desmond in the Maestro 2021-2 environment. Starting structures were obtained from the structural models described above. The System Builder tool was used to generate an orthorhombic simulation box with 10 Å boundaries on all sides. The simulation box was filled with water molecules using the TIP4PEW water model.[25] NaCl ions were added to achieve system neutrality and to reach a salt concentration of 0.15 M. Following equilibration, 100 ns production runs were completed using the OPLS4 force field.[26] Trajectories were prepared for analysis with VMD (version 1.9.4a55).[27] Data analysis was carried out with VMD and in-house code using the MDAnalysis Python package.[28,29] All trajectories showed minimal changes in RMSD values over the simulation times (Figures S24–S33). Hydrogen bond occupancy over each trajectory was measured using the Hydrogen Bonds Analysis extension in VMD with a donor:acceptor distance cutoff of 3.0 Å and an angle cutoff of 20°. Hydrogen bond occupancy was calculated as the percentage of time during which H-bonding criteria are met over the course of the trajectory. The script for interdimer contact angle calculations can be found on GitHub (https://github.com/ppistono).

Thermal Shift Assay. SYPRO orange thermal shift assays were conducted in triplicate in 96-well plates using a BioRad CFX Connect RT-PCR instrument. Temperatures were increased by 1 °C increments from 25 to 95 °C. During this process, the SYPRO orange dye binds to MS2 dimers as capsid disassembly and protein denaturation occurs. MS2 variants were tested for individual optimal assay conditions using 5, 10, 15, or 20 μM MS2 (by monomer concentration with 1× to 8× SYPRO orange dye). The best conditions for data collection were found to be 10 μM MS2 and 6× dye after assay optimization. For melting point determination, a Boltzmann sigmoidal model fit was employed using Prism-9, where T_m can be calculated as V_{50} (eq 2).[30] For all MS2 mutants, melt curve derivatives were analyzed using the Peakdetect module in Python. The T_m values are reported as mean and standard deviation of each set of replicates. Two melting points, T_m1 and T_m2, were observed in some data sets, suggesting that certain mutants exhibit cooperative melting profiles (Figure S6, Table S4).

$$Y = \text{Bottom} + \frac{\text{Top} - \text{Bottom}}{1 + e^{(V_{50} - X)/\text{Slope}}} \quad (2)$$

Transmission Electron Microscopy Sample Preparation. MS2 CP samples were spun down at 15k rpm for 15 min at 4 °C to remove aggregates. Dilute (1 mg/mL) MS2 samples were then concentrated and washed three times with 1× PBS through 0.5 mL Amicon Ultra 100 kDa MWCO filters at 15k rpm for 3 min at 4 °C. Washed samples were diluted back to a concentration of 1 mg/mL in 1x PBS and spun down at 15k rpm for 15 min at 4 °C. Finally, samples were filtered through a 0.2 μm spin filter at 15k rpm for 30 s.

Uranyl Acetate Negative Staining. A 1% uranyl acetate staining solution was spun down at 5000 rpm for 10 min to remove aggregates. Carbon-coated copper grids were glow discharged and 6 μL of MS2 samples were pipetted onto the grid, incubated for 2 min, then washed 3 times with MQ H_2O. Excess liquid was removed from each grid with filter paper. Grids were then stained with 6 μL of 1% uranyl acetate, incubated for 1 min, and excess stain removed with filter paper.

Transmission Electron Microscopy. TEM images were acquired on a Tecnai 12 Transmission Electron Microscope. Images were acquired at 30,000× and 49,000× magnification and particle size was measured using the Set Scale and Measure tools in Fiji (Figures S7–S23).

RESULTS AND DISCUSSION

Intersubunit Interface Mutations Control MS2 Particle Structure and Stability in Unanticipated Ways. In order to explore the effect of quaternary structure on the cellular uptake and stability properties of MS2 VLPs, we generated locally supercharged MS2 variants with all possible combinations of arginine and lysine at CP positions 71 and 73, with fixed S37P

https://doi.org/10.1021/acs.biochem.4c00225
Biochemistry 2024, 63, 1913–1924

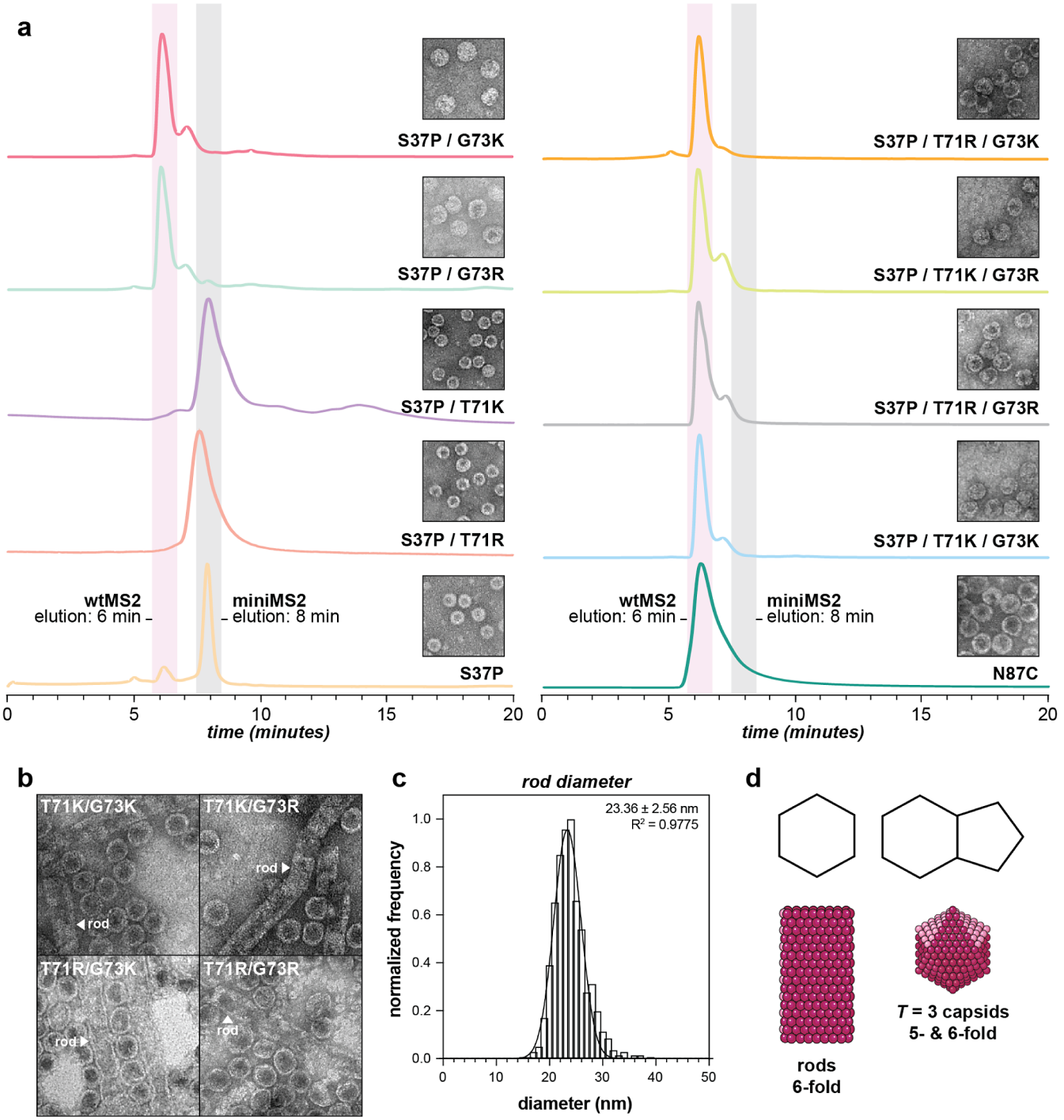

Figure 2. (A) HPLC SEC tryptophan fluorescence chromatograms of MS2 CP variants. Highlighted in pink is the expected elution time of assembled $T = 3$ capsids (6 min) and highlighted in gray is the expected elution time of assembled $T = 1$ capsids (8 min). All S37P variants also contain the N87C mutation. Shown as an inset on the right side of each chromatogram is a representative transmission electron microscopy (TEM) image of each MS2 CP variant. (B) TEM images of each MS2[N87C] double mutant showing a mixed population of rods and $T = 3$ particles. (C) The normalized frequency distribution of the measured MS2 rod diameters, reported as mean diameter ± one standard deviation. The data was fitted to a Gaussian distribution and the R^2 value is reported. (D) Diagrams showing the assembly geometries of a rod-shaped particle (left) made of only 6-fold assembly interfaces, and a $T = 3$ capsid (right) made of 5- and 6-fold assembly interfaces.

and N87C backbone point mutations. The specific mutants that were evaluated are listed in Figure 2A. The MS2[S37P] mutation was expected to shift the MS2 VLP assembly from a 27 nm, $T = 3$ icosahedron with 180 monomers to a 17 nm, $T = 1$ icosahedron with 60 monomers, with an interior cysteine [N87C] for bioconjugation.[17] All nine MS2[S37P/N87C] variants were expressed, and the assembly state of each variant was assessed via size exclusion chromatography (Figure 2A). All MS2[S37P/N87C] variants produced assembled capsids, and the elution times of MS2[S37P/N87C] variants with single mutations at position 71 corresponded to the expected 17 nm, $T = 1$ miniMS2 capsids.

https://doi.org/10.1021/acs.biochem.4c00225
Biochemistry 2024, 63, 1913−1924

In contrast, the elution times of MS2[S37P/N87C] variants with single mutations at position 73 or double mutations at position 71 and 73 corresponded to 27 nm, $T = 3$ capsids. These unexpected results were further confirmed via transmission electron microscopy (TEM). Images of each MS2 [S37P/N87C] CP mutant showed uniformly sized VLP populations. In contrast, TEM images of each MS2[N87C] mutant revealed the presence of extended rod-like structures with varying lengths and uniform 23.36 ± 2.56 nm diameters in addition to spherical $T = 3$ capsids in MS2[N87C] (Figure 2). This was only observed for all four samples with double mutations at both position 71 and position 73, and rods were not detected in any single mutant samples. Upon further analysis, we found that rod-like structures were absent in TEM images of freshly purified samples that were filtered and frozen before TEM grid preparation and imaging. However, rod-like structures were seen in images of freshly expressed, unfiltered *E. coli* cell lysate and in freshly purified, unfiltered MS2[N87C] double mutant capsids that were maintained at 4 °C over several days. Thus, the best 71*K*/73R and 71*R*/73K capsid mutants for cell uptake, identified in our previous studies, exhibited an assembly instability that can be rescued by adding the S37P mutation while maintaining the overall capsid size.

We assign the rod-like structures to a nonlength-controlled propagation of the 6-fold assembly interface. The presence of a mixed population of rod-like structures and $T = 3$ spheres in the MS2[N87C] double mutant samples suggests that the [T71K/G73R] mutation may destabilize interdimer interactions at the 5-fold assembly interface and/or produce favorable interactions at the 6-fold assembly interface. Disruption of assembly interface interactions through mutations such as loop insertions has been shown to produce mixed rod-like and spherical particles in Qβ VLPs via substitution of residues 76 to 81 in the FG loop.[13] Although the assembly of Qβ differs from that of MS2 by the presence of four disulfide bonds between residues 74 and 80, residues 76 to 81 in Qβ are analogous to residues 71 to 76 of MS2, where the FG loops converge at the 5-fold and 6-fold interfaces. The assembly of mixed rod-like and spherical particles has also been shown when reassembling mixtures of coat protein dimers *in vitro* from different RNA phages such as MS2, fr, and GA.[14]

The thermal shift assay results also provide evidence that the [N87C] double mutants are less stable than their [S37P/N87C] counterparts. The melting point (T_m) of wtMS2 has been reported to be ∼66 °C. While MS2[S37P] has similar stability, melting point assays also reported a second T_m of ∼77 °C, indicating a two-stage melting curve for miniMS2 capsids.[17,31] We assign the lower T_m to capsid disassembly and the higher T_m to monomer unfolding. Using a SYPRO Orange thermal shift assay, we measured the T_m of MS2[N87C] and MS2[S37P/N87C] as well as each variant with single and double mutations at positions 71 and 73 (Figures 3 and S6). The T_m trend for each MS2[N87C] double mutant matched our previously reported results in a dynamic light scattering (DLS)-based thermal shift assay, with T_m values ranging from 42 to 49 °C. This indicates that adding the cationic residues reduces stability compared to wtMS2. This aligns more closely with the hypothesis that the cationic residues destabilize the 5-fold axes relative to wtMS2.

The T_m values for each MS2[S37P/N87C] double mutant ranged from 53 to 59 °C, indicating particles with increased thermal stability compared to their [N87C] counterparts. For the MS2[S37P/N87C] single mutants, the measured T_m values ranged from 53 to 61 °C, with three of the four variants possessing a curve with a second T_m from 74 to 76 °C. These data confirm that the S37P mutation compensates for the loss in assembly stability caused by the cationic mutations discussed above. They also suggest that the original observation that MS2[S37P] forms $T = 1$ capsids may be due to the ability of the mutation to increase the stability of the 5-fold interfaces, making them the sole pattern that occurs in these capsids.

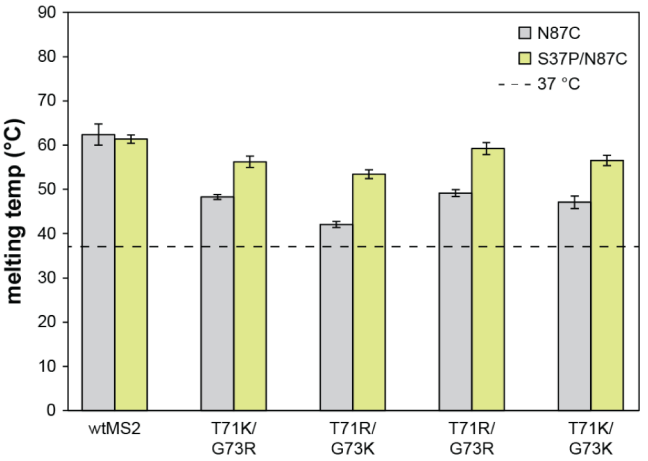

Figure 3. Bar graphs showing the mean melting temperature (T_m) of each MS2 variant in degrees Celsius (°C). Error bars shown one standard deviation. The measurements for the [N87C] and [S37P/N87C] versions of each MS2 variant are shown in gray and green, respectively. Physiologically relevant temperature (37 °C) is marked as a dashed line.

Molecular Dynamics Simulations Provide Insight into Particle Interface Interactions. To identify the possible structural and conformational changes that yield MS2[S37P/N87C] capsids with unexpected $T = 3$ architectures, a series of MS2 capsid variants was modeled *in silico*. MS2 variants with different combinations of mutations (wt, S37P, T71K/G73R, and S37P/T71K/G7R) were introduced into three geometrically and conformationally distinct starting structures based on six sets of wtMS2 coat protein dimers (CP2) at the 6-fold assembly interface (2MS2-6CP2, starting from PDB ID: 2MS2) and ten sets of wtMS2 CP dimers assembled at the 5-fold interface (10CP2, also from PDB ID: 2MS2) (Figure 4A–C). The same set of mutations was also introduced into ten sets of coat protein dimers of miniMS2 assembled at the 5-fold interface (4ZOR-10CP2, from PDB ID: 4ZOR) (Figure 4A–C). As noted in Figure 4, miniMS2 lacks 6-fold interfaces. The three partial MS2 assemblies that were used in molecular dynamics simulations are depicted in Figure 4A. The 6CP2 and 10CP2 input structures were previously identified as key intermediates in the MS2 capsid assembly pathway, and were used as inputs in *in silico* deep mutational scans of the wtMS2 and S37P MS2 coat proteins, enabling successful prediction of capsid self-assembly.[20,32]

The full capsid and complete virion of MS2 with its native genome have been studied using all-atom molecular dynamics, revealing useful information about RNA-capsid interactions.[33−35] However, full capsid all-atom simulations are computationally intensive, and corresponding coarse-grained simulations may not allow the study of interactions between specific residues or atoms. Given the biological relevance and smaller sizes of the 6CP2 and 10CP2 assembly intermediates, we decided to use these input structures for molecular dynamics simulations. A similar approach was used to design stabilized

https://doi.org/10.1021/acs.biochem.4c00225
Biochemistry 2024, 63, 1913−1924

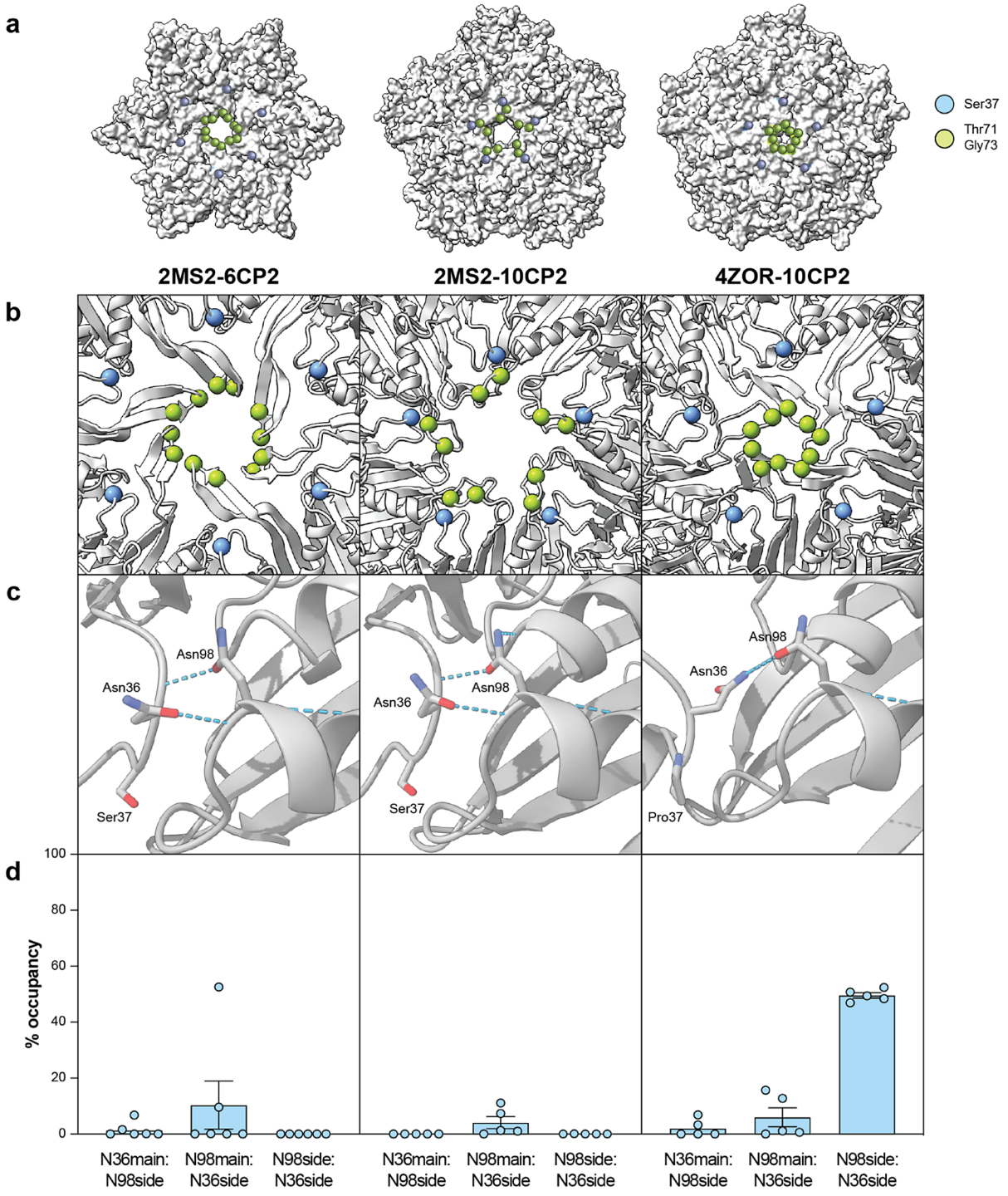

Figure 4. (A) Input structures for molecular dynamics simulations represent the minimal assembly intermediates at the 5-fold and 6-fold interfaces for wtMS2 and miniMS2. Structures are labeled with their PDB ID (wtMS2; 2MS2, miniMS2; 4ZOR) and assembly state (6CP2; 6 coat protein dimers, 10CP2; 10 coat protein dimers). Ser37 (blue) and Thr71/Gly73 (green) are labeled with spheres. (B) A closer view of the assembly interface for each input structure. (C) The key hydrogen bonding interactions between Asn36 and Asn98 at each assembly interface, with the H-bonds labeled by light blue dashed lines. (D) H-bonding interactions were measured over the course of a 100 ns trajectory. Bar graphs show the mean % H-bonding occupancy between Asn36 and Asn98 and error bars show one standard deviation. H-bonding interactions between the Asn36 backbone and Asn98 side chain (N36main:N98side), Asn98 backbone and Asn36 side chain (N98main:N36side), and Asn98 side chain and Asn36 side chain (N98side:N36side) are shown left to right. Each replicate measurement is shown as a blue circle on its respective graph.

foot-and-mouth disease (FMDV) virus capsids for vaccine design.[36] In that work, a library of pentamer interface mutants was created and molecular dynamics simulations were used to rank predicted stabilizing mutations. This study found that increased *in silico* and experimental stability correlated with mutation hydrophobicity.[36]

Previous structural studies of $T = 1$ miniMS2 capsids revealed a key decrease in the interdimer angles due to differences in hydrogen bonding at the dimer−dimer interface.[17] A switch to

https://doi.org/10.1021/acs.biochem.4c00225
Biochemistry 2024, 63, 1913−1924

the *cis*-amide conformation of Pro37 alters the configuration of neighboring residues, creating a new hydrogen-bonding interaction between the side-chain nitrogen of Asn36 and the side-chain oxygen of Asn98. This decreases the interdimer contact angle, leading to greater local curvature and, ultimately, a smaller capsid size.[17]

Through molecular dynamics simulations, we could recapitulate these differences in hydrogen bonding. By comparing hydrogen bonding contacts between Asn36 and Asn98 over each 100 ns trajectory, we observed substantial differences in the numbers and types of contacts for input structures with different mutations. Trajectories with the miniMS2 (10CP2-4ZOR) input structure had high (>49%) N98side:N36side H-bonding occupancy. In contrast, trajectories with the wtMS2 5-fold input structure (10CP2-2MS2) displayed no N98side:N36side interactions; instead, these structures exhibited a low to moderate (4 to 10%) N98backbone:N36side occupancy that was also present in the miniMS2 simulations (6%) (Figure 4D). Lower amounts of H-bonding contacts between N98side:N36side were observed in trajectories with the 6-fold input structure (6CP2-2MS2) versus trajectories with the 5-fold input structure (10CP2-2MS2) when comparing the same sets of mutations (Figure 5A). These *in silico* data support the previously reported structural hypothesis that a new hydrogen-bonding interaction between the side chains of N36 and N98 plays a major role in decreasing the interdimer contact angle, favoring a smaller, $T = 1$ capsid assembly.[17] We also measured the difference in the N98side:N36side when comparing 10CP2 input structures with *cis* versus *trans* proline at position 37 (Figure 5B,C). Trajectories with *cis* proline all had high % occupancy (47−50%), while trajectories with *trans* proline all had low or zero % occupancy (0−6%), suggesting that the conformation of proline at position 37 is an important factor in the stability of the 5-fold assembly interface (Figure 5D).

The interdimer contact angles were also measured over the course of each trajectory. The centers of mass of the neighboring residues 36 and 98 were calculated, and a vector was drawn to represent the axis between the residues in each neighboring dimer. Then, the angle between the two vectors over each trajectory was calculated and plotted. Similar to the H-bonding occupancy results, comparing the angles measured in 10CP2 structures with *cis* versus *trans* proline at position 37 resulted in a notable difference. Trajectories with *cis* proline at position 37 all had lower dimer interface angles (6°), while trajectories with *trans* proline all had higher dimer interface angles (12° to 14°) (Figure 5E). Assuming that Pro37 in a $T = 3$ icosahedron occupies a *cis* conformation, while Pro37 in a $T = 1$ icosahedron occupies a *trans* conformation, then these data align with the hypothesis that the interdimer angle in a $T = 1$ icosahedral structure will be smaller than the same angle measured in a $T = 3$ icosahedral structure.

Locally Supercharged S37P Mutants Retain Increased Cellular Uptake Properties. To assess the cellular uptake properties of locally supercharged MS2[S37P/N87C] variants, purified capsids were labeled by conjugation of Lissamine rhodamine B maleimide to the interior Cys87 residues on each monomer. Capsid concentrations were normalized to 5 μM, and U-251 MG glioblastoma cells were treated with labeled capsids for 1 h before flow cytometry analysis. The internalization results measured by mean rhodamine fluorescence matched the patterns seen in similar experiments using locally supercharged MS2[N87C] variants. Specifically, MS2 capsids with single cationic mutations at positions 71 and 73 showed no or very low

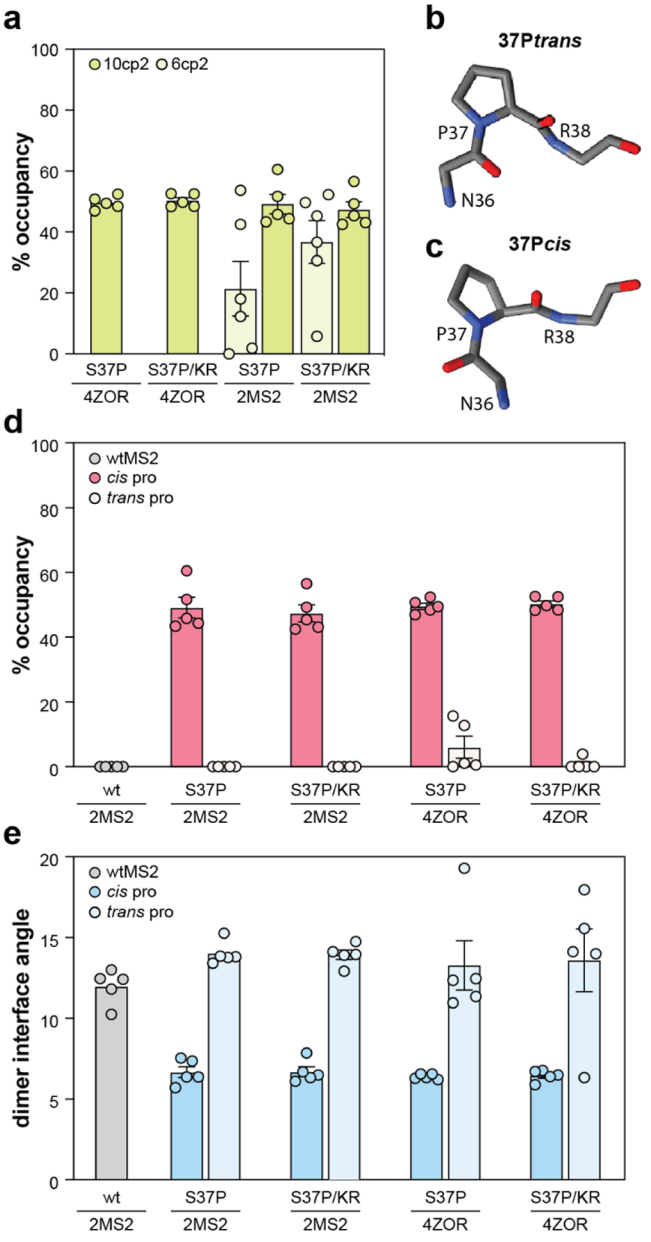

Figure 5. (A) Bar graph showing the mean % H-bonding occupancy of N98side:N36side interactions in different MS2 input structures. Error bars show SEM 6CP2 (light green) and 10CP2 (green) measurements are shown when applicable. Structures of residues 36−38 showing *trans* (B) and *cis* (C) proline at position 37. (D) Bar graph showing the mean % H-bonding occupancy of N98side:N36side interactions in different MS2 10CP2 input structures. *Cis* proline (pink) and *trans* proline (light pink) are shown. (E) Bar graph showing the mean dimer interface angle between N36 and N98 in different MS2 10CP2 input structures. *Cis* proline (blue) and *trans* proline (light blue) are shown.

cellular uptake, while all combinations of double Arg and Lys mutants at positions 71 and 73 show greatly increased fluorescence when compared to both untreated and MS2-[S37P]-treated cells (Figure 6). In this experiment, the best-performing variant, MS2[S37P/T71K/G73R/N87C], showed a mean fluorescence intensity that was 55-fold higher than cells treated with MS2[S37P].

These cellular internalization studies indicated that locally supercharged MS2[S37P/N87C] capsids performed just as well as our previously reported MS2[N87C] capsids with analogous

https://doi.org/10.1021/acs.biochem.4c00225
Biochemistry 2024, 63, 1913−1924

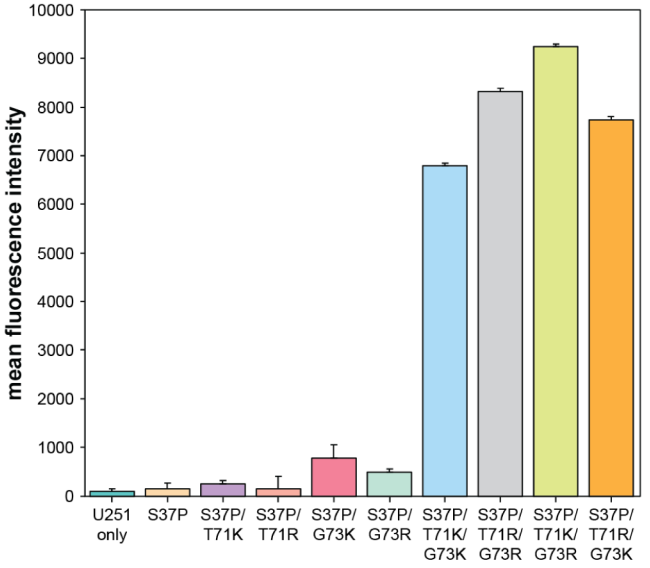

Figure 6. Bar graphs showing corrected mean fluorescence intensity of MS2-Lissamine rhodamine B internalization into U-251 MG cells. Error bars show the coefficient of variation. Data shown are a concatenation of three biological replicates as measured by flow cytometry.

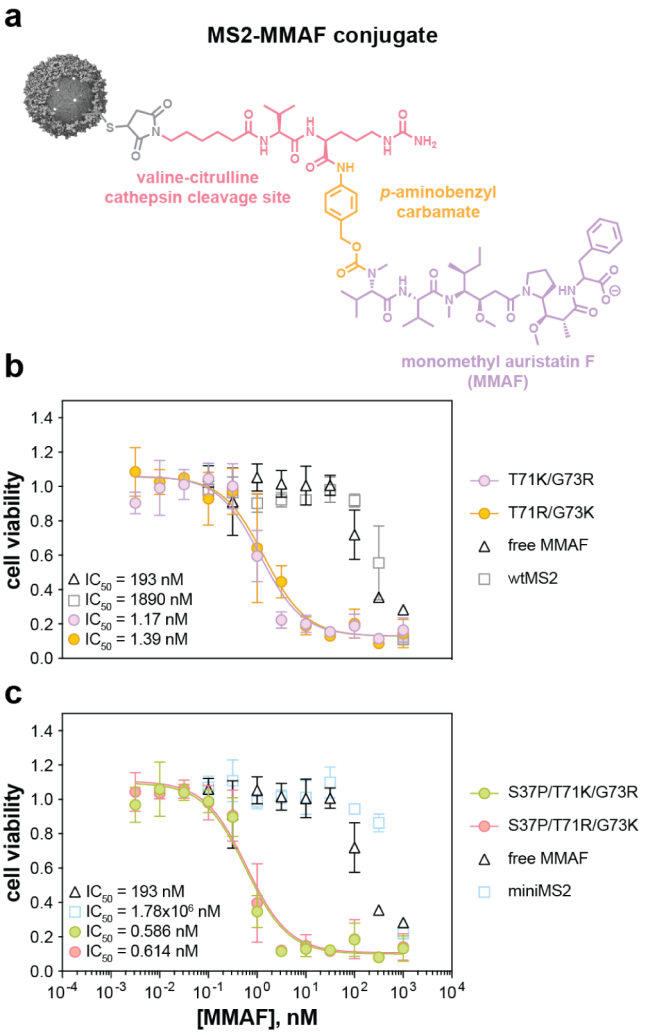

Figure 7. (A) Structure of the MS2-MMAF conjugate. MS2 capsid with an interior cysteine conjugated to maleimide handle (gray), Val-Cit linker (pink), *p*-aminobenzyl carbamate linker (orange), and MMAF (purple). (B), (C) MS2-MMAF dose response assays for MS2[N87C] variants and MS2[S37P/N87C] variants, respectively. Results are shown for an MTS assay of U-251 MG cells 72h after treatment with.003−1000 nM MMAF. Plot shows mean % cell viability of three biological replicates. Error bars shown one standard deviation.

mutations, with the added advantage of having single, thermally stable $T = 3$ assembly states. It is unclear how the formation of MS2 rod-like structures affects cellular internalization and if these rods are taken up into mammalian cells along with the $T = 3$ icosahedral particles. Unfortunately, we have not yet been able to create $T = 1$ miniMS2 capsids that retain the same combinations of cellular uptake-enhancing mutations and study the effects of particle size on internalization. Previous work by other groups has explored the shape and size dependence of viral uptake using tobacco mosaic virus (TMV) and cowpea chlorotic mottle virus (CCMV). Some studies have suggested that materials with high aspect ratios (rod-like and filamentous structures) are internalized by cells differently than materials with low aspect ratios (spheres); however, these studies did not look into the difference of differently sized particles with the same aspect ratio (e.g., $T = 3$ versus $T = 1$ particles).[37−40]

Locally Supercharged MS2 and MS2[S37P] Variants Enable Intracellular Delivery of MMAF *In Vitro*. We next compared the delivery efficacy of a small molecule drug conjugated to the interior of locally supercharged MS2 (T71K/G73R) versus the stabilized mutant possessing S37P (S37P/T71K/G73R). Monomethyl auristatin E (MMAE) and monomethyl auristatin F (MMAF) are powerful anticancer drugs that block tubulin polymerization and inhibit cell division. These drugs are generally used in conjugates with monoclonal antibodies (mAbs) to create antibody-drug conjugates (ADCs) with targeted cytotoxicity. THIOMABs with engineered cysteines have been developed for the conjugation of cysteine-reactive drug molecules, such as maleimides, to antibodies.[41] An enzyme-cleavable dipeptide Val-Cit linker is used to allow for cleavage and release of the free drug by the cathepsin B lysosomal protease upon cell entry (Figure 7A).[42−44] MMAE and MMAF are structurally similar and are both expected to bind to tubulin with similar affinities, but exhibit different membrane permeabilities due to the presence of a negatively charged carboxylic acid group on MMAF. Therefore, we hypothesized that the delivery of MMAF would be improved by conjugation to the interior of MS2, given its ability to load up to 180 drug copies per capsid and shield its negative charge from the anionic mammalian cell exterior. Maleimide-Val-Cit-PAB-MMAF was conjugated to the interior cysteine of wtMS2, miniMS2, and all combinations of MS2 T71K/G73R and T71R/G73K with and without the stabilizing S37P mutation. Each MS2 CP variant was modified to 86−93% by monomer with MMAF or about 154−168 molecules per capsid (Figure S5, Table S3).

The efficacy of MS2-MMAF was measured by a dose−response assay in U-251 MG cells. Cells were treated for 72 h with up to 1000 nM MMAF conjugated to each of six MS2 variants. The calculated IC_{50} values for MMAF treatment with each MS2 variant are shown in Figure 7. These data show that MMAF delivery with locally supercharged variants results in a drastic increase in efficacy versus delivery of MMAF with wtMS2 or miniMS2 and up to a 328-fold increase in efficacy versus delivery of free MMAF. Although no significant difference in

https://doi.org/10.1021/acs.biochem.4c00225
Biochemistry 2024, 63, 1913−1924

efficacy was observed when comparing MS2 variants with versus without the stabilizing S37P mutation, these capsids are still a valuable addition to the MS2 drug delivery arsenal due to their structural homogeneity and ease of storage.

CONCLUSION

Previous work has established that VLP assembly states can be modified via simple point mutations, providing a platform for creating particles with fine-tuned sizes, stabilities, and other properties. By using a combination of experimental techniques and molecular dynamics simulations, this work explores how specific mutations at the intersubunit interfaces of MS2 impact the local and global structure and function of these capsids. Notably, we reveal that placing cationic mutations at critical interface residues can induce unexpected changes in particle geometry, leading to the formation of rod-like structures alongside capsids with expected assembly states. When combined with the 5-fold-favoring S37P mutation, we observe VLPs with an unexpected $T = 3$ assembly state, improved thermostability, and retained enhancement of cellular uptake properties. Molecular dynamics experiments further explain these findings, providing structural insights at the atomistic level into the importance of intradimer hydrogen bonding interactions on global capsid structure and assembly. Additionally, we demonstrate the efficacy of these engineered VLPs in delivering the anionic small-molecule drug MMAF, achieving up to 300-fold increases in potency over the free drug. This showcases the potential of these engineered capsids for biomedical applications. Moreover, these results highlight the importance of understanding the sequence-structure relationship of self-assembling, protein-based materials such as VLPs in order to improve their potential for applications such as drug delivery.

ASSOCIATED CONTENT

Supporting Information

The Supporting Information is available free of charge at https://pubs.acs.org/doi/10.1021/acs.biochem.4c00225.

All mass spectra, transmission electron microscopy images, and supplementary figures and tables (PDF)

Accession Codes

2MS2 and 4ZOR: P03612 (UniProt)

AUTHOR INFORMATION

Corresponding Author

Matthew B. Francis − *Department of Chemistry, University of California, Berkeley, California 94720, United States; Materials Sciences Division, Lawrence Berkeley National Laboratory, Berkeley, California 94720, United States;* orcid.org/0000-0003-2837-2538; Email: mbfrancis@berkeley.edu

Authors

Paige E. Pistono − *Department of Chemistry, University of California, Berkeley, California 94720, United States*

Junyi Xu − *Department of Chemistry, University of California, Berkeley, California 94720, United States*

Paul Huang − *Department of Chemistry, University of California, Berkeley, California 94720, United States;* orcid.org/0000-0002-3520-0032

Jennifer L. Fetzer − *Department of Chemistry, University of California, Berkeley, California 94720, United States*

Complete contact information is available at: https://pubs.acs.org/10.1021/acs.biochem.4c00225

Notes

The authors declare the following competing financial interest(s): P.P., P.H., and M.B.F. are named inventors of a pending patent application related to the work described.

ACKNOWLEDGMENTS

This work was supported by the Panattoni Family Fund and the NSF (2044011). Computational studies in this work were completed with support from the UC Berkeley MGCF and NIH S10OD023532. We are grateful to M. West, manager at the QB3 CTAF, for qPCR and flow cytometry training, and R. Zalpuri at the UC Berkeley EML for negative staining and transmission electron microscopy training.

ABBREVIATIONS

VLP, virus-like particle; wt, wild-type; HPLC, high-performance liquid chromatography; FPLC, fast protein liquid chromatography; LC/QTOF, liquid chromatography quadrupole time-of-flight; QTOF-ESI-MS, quadrupole time-of-flight electrospray ionization mass spectrometry; MWCO, molecular weight cutoff; SDS-PAGE, sodium dodecyl sulfate polyacrylamide gel electrophoresis; DMSO, dimethyl sulfoxide; CP, coat protein; TEM, transmission electron microscopy; T_m, melting temperature; TMV, tobacco mosaic virus; CCMV, cowpea chlorotic mottle virus; SEM, standard error of the mean; MMAE, monomethyl auristatin E; MMAF, monomethyl auristatin F; ADC, antibody drug conjugate; mAb, monoclonal antibody; MG, malignant glioma

REFERENCES

(1) Wen, A. M.; Steinmetz, N. F. Design of Virus-Based Nanomaterials for Medicine, Biotechnology, and Energy. *Chem. Soc. Rev.* **2016**, *45* (15), 4074−4126.

(2) Dedeo, M. T.; Finley, D. T.; Francis, M. B. Chapter 8 - Viral Capsids as Self-Assembling Templates for New Materials. In *Molecular Assembly in Natural and Engineered Systems*, Howorka, S., Ed.; Academic Press, 2011; Vol. *103*, pp. 353392. .

(3) Lobba, M. J.; Fellmann, C.; Marmelstein, A. M.; Maza, J. C.; Kissman, E. N.; Robinson, S. A.; Staahl, B. T.; Urnes, C.; Lew, R. J.; Mogilevsky, C. S.; Doudna, J. A.; Francis, M. B Site-Specific Bioconjugation through Enzyme-Catalyzed Tyrosine−Cysteine Bond Formation. *ACS Cent. Sci.* **2020**, *6* (9), 1564−1571.

(4) Brauer, D. D.; Hartman, E. C.; Bader, D. L. V.; Merz, Z. N.; Tullman-Ercek, D.; Francis, M. B. Systematic Engineering of a Protein Nanocage for High-Yield, Site-Specific Modification. *J. Am. Chem. Soc.* **2019**, *141* (9), 3875−3884.

(5) Maza, J. C.; Bader, D. L. V.; Xiao, L.; Marmelstein, A. M.; Brauer, D. D.; ElSohly, A. M.; Smith, M. J.; Krska, S. W.; Parish, C. A.; Francis, M. B. Enzymatic Modification of N-Terminal Proline Residues Using Phenol Derivatives. *J. Am. Chem. Soc.* **2019**, *141* (9), 3885−3892.

(6) Maza, J. C.; Ramsey, A. V.; Mehare, M.; Krska, S. W.; Parish, C. A.; Francis, M. B. Secondary Modification of Oxidatively-Modified Proline N-Termini for the Construction of Complex Bioconjugates. *Org. Biomol. Chem.* **2020**, *18* (10), 1881−1885.

(7) Bird, R. E.; Lemmel, S. A.; Yu, X.; Zhou, Q. A. Bioorthogonal Chemistry and Its Applications. *Bioconjugate Chem.* **2021**, *32* (12), 2457−2479.

(8) Caspar, D. L.; Klug, A. Physical Principles in the Construction of Regular Viruses. *Cold Spring Harb. Symp. Quant. Biol.* **1962**, *27*, 1−24.

(9) Twarock, R.; Luque, A. Structural Puzzles in Virology Solved with an Overarching Icosahedral Design Principle. *Nat. Commun.* **2019**, *10* (1), 4414.

(10) Chang, J.-Y.; Gorzelnik, K. V.; Thongchol, J.; Zhang, J. Structural Assembly of Qbeta Virion and Its Diverse Forms of Virus-like Particles. *Viruses* **2022**, *14* (2), 225.
(11) Garrido, N. D. M.; Crone, M. A.; Ramlaul, K.; Simpson, P. A.; Freemont, P. S.; Aylett, C. H. S. Bacteriophage MS2 Displays Unreported Capsid Variability Assembling T = 4 and Mixed Capsids. *Mol. Microbiol.* **2020**, *113* (1), 143−152.
(12) Biela, A. P.; Naskalska, A.; Fatehi, F.; Twarock, R.; Heddle, J. G. Programmable Polymorphism of a Virus-like Particle | Communications Materials. *Commun. Mater.* **2022**, *3* (1), 7.
(13) Cielens, I.; Ose, V.; Petrovskis, I.; Strelnikova, A.; Renhofa, R.; Kozlovska, T.; Pumpens, P. Mutilation of RNA Phage Qbeta Virus-like Particles: From Icosahedrons to Rods. *FEBS Lett.* **2000**, *482* (3), 261−264.
(14) Rumnieks, J.; Ose, V.; Tars, K.; Dislers, A.; Strods, A.; Cielens, I.; Renhofa, R. Assembly of Mixed Rod-like and Spherical Particles from Group I and II RNA Bacteriophage Coat Proteins. *Virology* **2009**, *391* (2), 187−194.
(15) Ni, C.-Z.; Syed, R.; Kodandapani, R.; Wickersham, J.; Peabody, D. S.; Ely, K. R. Crystal Structure of the MS2 Coat Protein Dimer: Implications for RNA Binding and Virus Assembly. *Structure* **1995**, *3* (3), 255−263.
(16) Hartman, E. C.; Jakobson, C. M.; Favor, A. H.; Lobba, M. J.; Álvarez-Benedicto, E.; Francis, M. B.; Tullman-Ercek, D. Quantitative Characterization of All Single Amino Acid Variants of a Viral Capsid-Based Drug Delivery Vehicle. *Nat. Commun.* **2018**, *9* (1), 1385.
(17) Asensio, M. A.; Morella, N. M.; Jakobson, C. M.; Hartman, E. C.; Glasgow, J. E.; Sankaran, B.; Zwart, P. H.; Tullman-Ercek, D. A Selection for Assembly Reveals That a Single Amino Acid Mutant of the Bacteriophage MS2 Coat Protein Forms a Smaller Virus-like Particle. *Nano Lett.* **2016**, *16* (9), 5944−5950.
(18) Robinson, S. A.; Hartman, E. C.; Ikwuagwu, B. C.; Francis, M. B.; Tullman-Ercek, D. Engineering a Virus-like Particle to Display Peptide Insertions Using an Apparent Fitness Landscape. *Biomacromolecules* **2020**, *21* (10), 4194−4204.
(19) Hartman, E. C.; Lobba, M. J.; Favor, A. H.; Robinson, S. A.; Francis, M. B.; Tullman-Ercek, D. Experimental Evaluation of Coevolution in a Self-Assembling Particle. *Biochemistry* **2019**, *58* (11), 1527−1538.
(20) Brauer, D. D.; Santiago, C. B.; Merz, Z. N.; McCarthy, E.; Tullman-Ercek, D.; Francis, M. B. Comprehensive Fitness Landscape of a Multi-Geometry Protein Capsid Informs Machine Learning Models of Assembly. *bioRxiv* **2021**.
(21) Ikwuagwu, B.; Hartman, E.; Mills, C. E.; Tullman-Ercek, D. Systematic Engineering of Virus-like Particles to Identify Self-Assembly Rules for Shifting Particle Size. *Virology* **2023**, *579*, 137−147.
(22) Hietpas, R. T.; Jensen, J. D.; Bolon, D. N. A. Experimental Illumination of a Fitness Landscape. *Proc. Natl. Acad. Sci. U. S. A.* **2011**, *108* (19), 7896−7901.
(23) Pistono, P. E.; Huang, P.; Brauer, D. D.; Francis, M. B. Fitness Landscape-Guided Engineering of Locally Supercharged Virus-like Particles with Enhanced Cell Uptake Properties. *ACS Chem. Biol.* **2022**, *17*, 3367.
(24) Valegård, K.; Liljas, L.; Fridborg, K.; Unge, T. The Three-Dimensional Structure of the Bacterial Virus MS2. *Nature* **1990**, *345* (6270), 36−41.
(25) Horn, H. W.; Swope, W. C.; Pitera, J. W.; Madura, J. D.; Dick, T. J.; Hura, G. L.; Head-Gordon, T. Development of an Improved Four-Site Water Model for Biomolecular Simulations: TIP4P-Ew. *J. Chem. Phys.* **2004**, *120* (20), 9665−9678.
(26) Lu, C.; Wu, C.; Ghoreishi, D.; Chen, W.; Wang, L.; Damm, W.; Ross, G. A.; Dahlgren, M. K.; Russell, E.; Von Bargen, C. D.; Abel, R.; Friesner, R. A.; Harder, E. D. OPLS4: Improving Force Field Accuracy on Challenging Regimes of Chemical Space. *J. Chem. Theory Comput.* **2021**, *17* (7), 4291−4300.
(27) Humphrey, W.; Dalke, A.; Schulten, K. V. Visual Molecular Dynamics. *J. Mol. Graph.* **1996**, *14* (1), 33−38.
(28) Gowers, R. J.; Linke, M.; Barnoud, J.; Reddy, T. J. E.; Melo, M. N.; Seyler, S. L.; Domański, J.; Dotson, D. L.; Buchoux, S.; Kenney, I. M.; Beckstein, O. MDAnalysis: A Python Package for the Rapid Analysis of Molecular Dynamics Simulations. *Proceedings Of The 15th Python In Science Conference*; U.S. Department of Energy Office of Scientific and Technical Information, 2016; 98105.
(29) Michaud-Agrawal, N.; Denning, E. J.; Woolf, T. B.; Beckstein, O. MDAnalysis: A Toolkit for the Analysis of Molecular Dynamics Simulations. *J. Comput. Chem.* **2011**, *32* (10), 2319−2327.
(30) GraphPad Prism 10 Curve Fitting Guide - Equation: Boltzmann sigmoid.
(31) Stonehouse, N. J.; Stockley, P. G. Effects of Amino Acid Substitution on the Thermal Stability of MS2 Capsids Lacking Genomic RNA. *FEBS Lett.* **1993**, *334* (3), 355−359.
(32) Knapman, T. W.; Morton, V. L.; Stonehouse, N. J.; Stockley, P. G.; Ashcroft, A. E. Determining the Topology of Virus Assembly Intermediates Using Ion Mobility Spectrometry−Mass Spectrometry. *Rapid Commun. Mass Spectrom.* **2010**, *24* (20), 3033−3042.
(33) Farafonov, V. S.; Nerukh, D. MS2 Bacteriophage Capsid Studied Using All-Atom Molecular Dynamics. *Interface Focus* **2019**, *9* (3), 20180081.
(34) Farafonov, V. S.; Stich, M.; Nerukh, D. A. Complete Virion Simulated: All-Atom Model of an MS2 Bacteriophage with Native Genome. *J. Chem. Theory Comput.* **2023**, *19* (21), 7924−7933.
(35) Farafonov, V. S.; Stich, M.; Nerukh, D. Reconstruction and Validation of Entire Virus Model with Complete Genome from Mixed Resolution Cryo-EM Density. *Faraday Discuss.* **2022**, *240*, 152−167.
(36) Kotecha, A.; Seago, J.; Scott, K.; Burman, A.; Loureiro, S.; Ren, J.; Porta, C.; Ginn, H. M.; Jackson, T.; Perez-Martin, E.; Siebert, C. A.; Paul, G.; Huiskonen, J. T.; Jones, I. M.; Esnouf, R. M.; Fry, E. E.; Maree, F. F.; Charleston, B.; Stuart, D. I. Structure-Based Energetics of Protein Interfaces Guides Foot-and-Mouth Disease Virus Vaccine Design. *Nat. Struct. Mol. Biol.* **2015**, *22* (10), 788−794.
(37) Shukla, S.; Eber, F. J.; Nagarajan, A. S.; DiFranco, N. A.; Schmidt, N.; Wen, A. M.; Eiben, S.; Twyman, R. M.; Wege, C.; Steinmetz, N. F. The Impact of Aspect Ratio on the Biodistribution and Tumor Homing of Rigid Soft-Matter Nanorods. *Adv. Healthcare Mater.* **2015**, *4* (6), 874−882.
(38) Arnida; Malugin, A; Ghandehari, H. Cellular Uptake and Toxicity of Gold Nanoparticles in Prostate Cancer Cells: A Comparative Study of Rods and Spheres. *J. Appl. Toxicol.* **2010**, *30* (3), 212−217.
(39) Liu, X.; Wu, F.; Tian, Y.; Wu, M.; Zhou, Q.; Jiang, S.; Niu, Z. Size Dependent Cellular Uptake of Rod-like Bionanoparticles with Different Aspect Ratios. *Sci. Rep.* **2016**, *6* (1), 24567.
(40) de Ruiter, M. V.; van der Hee, R. M.; Driessen, A. J. M.; Keurhorst, E. D.; Hamid, M.; Cornelissen, J. J. L. M. Polymorphic Assembly of Virus-Capsid Proteins around DNA and the Cellular Uptake of the Resulting Particles. *J. Controlled Release* **2019**, *307*, 342−354.
(41) Junutula, J. R.; Raab, H.; Clark, S.; Bhakta, S.; Leipold, D. D.; Weir, S.; Chen, Y.; Simpson, M.; Tsai, S. P.; Dennis, M. S.; Lu, Y.; Meng, Y. G.; Ng, C.; Yang, J.; Lee, C. C.; Duenas, E.; Gorrell, J.; Katta, V.; Kim, A.; McDorman, K.; Flagella, K.; Venook, R.; Ross, S.; Spencer, S. D.; Lee Wong, W.; Lowman, H. B.; Vandlen, R.; Sliwkowski, M. X.; Scheller, R. H.; Polakis, P.; Mallet, W. Site-Specific Conjugation of a Cytotoxic Drug to an Antibody Improves the Therapeutic Index. *Nat. Biotechnol.* **2008**, *26* (8), 925−932.
(42) Okeley, N. M.; Miyamoto, J. B.; Zhang, X.; Sanderson, R. J.; Benjamin, D. R.; Sievers, E. L.; Senter, P. D.; Alley, S. C. Intracellular Activation of SGN-35, a Potent Anti-CD30 Antibody-Drug Conjugate. *Clin. Cancer Res.* **2010**, *16* (3), 888−897.
(43) Doronina, S. O.; Toki, B. E.; Torgov, M. Y.; Mendelsohn, B. A.; Cerveny, C. G.; Chace, D. F.; DeBlanc, R. L.; Gearing, R. P.; Bovee, T. D.; Siegall, C. B.; Francisco, J. A.; Wahl, A. F.; Meyer, D. L.; Senter, P. D. Development of Potent Monoclonal Antibody Auristatin Conjugates for Cancer Therapy. *Nat. Biotechnol.* **2003**, *21* (7), 778−784.
(44) Sutherland, M. S. K.; Sanderson, R. J.; Gordon, K. A.; Andreyka, J.; Cerveny, C. G.; Yu, C.; Lewis, T. S.; Meyer, D. L.; Zabinski, R. F.; Doronina, S. O.; Senter, P. D.; Law, C.-L.; Wahl, A. F Lysosomal Trafficking and Cysteine Protease Metabolism Confer Target-Specific

https://doi.org/10.1021/acs.biochem.4c00225
Biochemistry 2024, 63, 1913−1924

Cytotoxicity by Peptide-Linked Anti-CD30-Auristatin Conjugates *. *J. Biol. Chem.* **2006**, *281* (15), 10540−10547.

https://doi.org/10.1021/acs.biochem.4c00225
Biochemistry 2024, 63, 1913−1924